



Biases in the Tropical Indian Ocean subsurface temperature variability in a coupled model

Rashmi Kakatkar^{1,2} · C. Gnanaseelan¹ · Jasti S. Chowdary¹ · J. S. Deepa^{1,2} · Anant Parekh¹

Received: 9 April 2018 / Accepted: 17 September 2018 / Published online: 20 September 2018
© Springer-Verlag GmbH Germany, part of Springer Nature 2018

Abstract

In this study, the subsurface temperature variability in the Tropical Indian Ocean (TIO) is examined in the Climate Forecast System version 2 (CFSv2) coupled model. The observations and reanalysis show a north–south dominant mode of variability in the TIO subsurface temperature during September–November, the season when the dominant east–west surface mode (Indian Ocean Dipole; IOD) peaks. The nature of the north–south dipole in TIO subsurface temperature is successfully captured by CFSv2. The observations however indicate that this subsurface mode, in general, persists for the next two seasons with stronger signals during December–February, whereas such tenacity is not seen in the model, instead rapid decay of the mode is seen in the model. It is found that the misrepresentation of both equatorial surface wind anomalies and associated Ekman transport as well as the Ekman pumping in the model have close association with the early weakening of the mode in CFSv2. The surface easterlies are generally modulated by the presence of twin anticyclones on both sides of the equator. The model captured these anticyclones with weaker than observed intensity and the northern anticyclone is confined over much smaller region than observed. Association of the subsurface mode with El Niño Southern Oscillation (ENSO) and IOD is further examined in this study. The anomalously prolonged decay phase of El Niño in CFSv2 is found only during the El Niño, IOD co-occurrence years, which was not reported before. This paves way for addressing an important modeling issue which is common in many coupled climate models including CFSv2. The analysis suggests the possible role of coupled air–sea interaction over the TIO on the El Niño cycle in the Pacific. It is also found that the misrepresentation of subsurface variability in CFSv2 during December–February is closely associated with the rapid decay of El Niño forced TIO warming.

1 Introduction

The subsurface variability in the Tropical Indian Ocean (TIO) is a topic of great interest because of its impact on the surface variability. In the Pacific Ocean, sea surface temperature (SST) and subsurface temperature are closely associated with El Niño–Southern Oscillation (ENSO) and show co-variability. On the contrary, in TIO, the dominant modes (subsurface and surface) do not show co-variability (e.g., Rao et al. 2002; Sayantani and Gnanaseelan 2015). The first dominant mode of SST variability in the TIO is the basin wide warming/cooling pattern associated with ENSO (e.g.,

Klein et al. 1999; Yang et al. 2007; Chowdary and Gnanaseelan 2007). However, the forcing mechanisms responsible for this are still under debate. One school advocates ENSO induced basin wide TIO SST warming as a response mainly through atmospheric fluxes (e.g. Klein et al. 1999; Lau and Nath 2000; Alexander et al. 2002), while several studies stressed the importance of oceanic Rossby waves for both the formation and its evolution especially for the persistent warming of southern TIO (STIO) (Masumoto and Meyers 1998; Chambers et al. 1999; Xie et al. 2002; Chakravorty et al. 2014).

The leading mode of subsurface temperature variability in the TIO shows a dipole structure (Chambers et al. 1999; Feng et al. 2001; Rao et al. 2002; Xie et al. 2002; Feng and Meyers 2003; Shinoda et al. 2004; Sayantani and Gnanaseelan 2015). This subsurface dipole is forced by both ENSO and Indian Ocean Dipole (IOD). The role of Indian Ocean (IO) as well as the Pacific Ocean on the generation and maintenance of Rossby waves in STIO

✉ C. Gnanaseelan
seelan@tropmet.res.in

¹ Indian Institute of Tropical Meteorology, Pune 411008, India

² Department of Atmospheric and Space Sciences, Savitribai Phule Pune University, Pune, India

has been discussed by many researchers (e.g. Chambers et al. 1999; Xie et al. 2002; Rao et al. 2002; Rao and Behera 2005; Chowdary and Gnanaseelan 2007; Vaid et al. 2007; Gnanaseelan et al. 2008; Chowdary et al. 2009; Gnanaseelan and Vaid 2010; Chakravorty et al. 2013, 2014; Sayantani and Gnanaseelan 2015, etc). Previous studies analysed the composites of IOD, El Niño and the IOD-El Niño co-occurrence years to examine the relative impact of these two forcing on TIO inter-annual variability. Rao et al. (2002) reported that the subsurface variability in TIO is an east–west dipole pattern associated with IOD. They reported that the ocean dynamics modulated by equatorial zonal winds is important for the generation of dipole pattern. Yu et al. (2005) discussed the origins of inter-annual thermocline variations in the TIO. They noted that variations north of 10°S are associated with IOD and south of 10°S are associated with ENSO, this is consistent with findings of several other studies (e.g. Saji et al. 1999; Rao and Behera 2005; Tozuka et al. 2010; Yokoi et al. 2012). Chakravorty et al. (2014) used ocean–atmosphere coupled model experiments to study the relative role of El Niño and IOD forcing on STIO Rossby waves. They suggested that the generation and maintenance of Rossby waves in STIO from boreal summer to fall is mainly through local ocean–atmosphere coupled processes. The intensification and maintenance of these waves after fall till the following spring are found to be due to remote forcing from Pacific. The north–south subsurface mode (Sayantani and Gnanaseelan 2015) is found to evolve in September–November (SON) and is closely associated with IOD forcing, but surprisingly intensifies in the following season with peak amplitudes in December–February (DJF), i.e. a season after the IOD forcing ceased. The signals are in fact maintained till March–May (MAM) of the following year. It is shown that this mode is generated due to the internal mode of variability of TIO forced by IOD but modulated by the remote forcing from the Pacific.

The subsurface-surface feedback in TIO is reported by several studies. Using in-situ measurements as well as from reanalysis data, Xie et al. (2002) showed that the coupled Rossby waves give potential predictability for SST in the south-western TIO (SWTIO), due to their coherent evolution. The downwelling Rossby waves and their upward propagation in the SWTIO induce surface warming over the SWTIO, which then modulates air–sea interaction locally (e.g., Chowdary et al. 2009). Deshpande et al. (2014) also studied the thermocline-SST coupling and the associated air–sea interaction especially during the strong IOD years. The subsurface temperature variations therefore could influence the surface temperature, thereby affecting the air–sea interactions and modulating the regional climate over the TIO (e.g.

Krishnan et al. 2006). Therefore, proper representation of subsurface temperature variations in coupled models is important to minimize the errors in the seasonal prediction (e.g., Srinivas et al. 2018). This has motivated us to understand the TIO subsurface variability in the coupled model, Climate Forecast System version 2 (CFSv2), which is an operational model used under the National Monsoon Mission of India for dynamical monsoon prediction (http://www.tropmet.res.in/monsoon/index_1.php). It is essential to evaluate the ability of CFSv2 in representing the TIO subsurface temperature variations and associated air–sea interactions. The present study addresses in particular, how CFSv2 represents the north–south/subsurface mode of variability, the associated mechanisms and the major climate modes such as ENSO and IOD. The paper is organized as follows. Data used in the study and methodology adopted for the analysis are described in Sect. 2. The subsurface mode in the model is addressed in Sect. 3. The reasons behind prior/early termination of subsurface mode in CFSv2 are discussed in Sect. 4. Representation of major climate modes over the tropical Indo Pacific in CFSv2 is explained in Sect. 5. Subsurface surface interaction in model and observations is discussed in Sect. 6. The summary is provided in Sect. 7.

2 Data and methodology

The National Centres for Environmental Prediction (NCEP)—CFSv2 is a coupled ocean–atmosphere–land model with advanced physics (Saha et al. 2014). The atmospheric component, NCEP Global Forecast System (GFS), the oceanic component, Modular Ocean Model version 4 (MOM4) (Griffies et al. 2004) from the Geophysical Fluid Dynamics Laboratory (GFDL), and a four layer Noah land-surface model (Ek et al. 2003) are coupled in CFSv2. GFS model has the horizontal resolution T126 and 64 sigma layers. MOM4 has 0.5° zonal resolution and 0.25° meridional resolution between 10°S and 10°N and decreases with latitudes to 0.5° poleward of 30°S and 30°N. It has 40 vertical layers with 27 layers in the upper 400 m. The vertical resolution from the surface to 240 m is 10 m and which decreases to 511 m in the bottom layer. The model is integrated over 100 years and the last 60 years of free simulations are used for the present study. The details of CFSv2 integrations are provided in Roxy (2014).

Ocean Reanalysis System 4 (ORAS4) monthly data of potential temperature from 1958 to recent available month (November 2017) is used in this study. This reanalysis is implemented at the European Centre for Medium-Range

Weather Forecasts (ECMWF) and is found to be performing better over the globe (Balmaseda et al. 2015) and IO in particular (Karmakar et al. 2018) compared to rest of the ocean reanalysis. ORAS4 reanalysis is based on the NEMO ocean model and the data assimilation system is NEMOVAR in 3D-Var FGAT mode. ORAS4 assimilates temperature and salinity profiles from the EN3 v2a XBT bias corrected database (1958–2009), including XBTs, CTDs, Moorings, Array for Real-Time Geostrophic Oceanography (ARGO) profiles and along track altimeter sea level anomalies and trends etc. NEMO model is forced by the ERA-40 reanalysis (Uppala et al. 2005) and ERA-Interim reanalysis (Dee et al. 2011) daily fluxes (Balmaseda et al. 2013) and so the winds and mean sea level pressure (mslp) data from ECMWF—ERA 40 reanalysis (1958–1978) and ERA-Interim reanalysis (1979–2017) are used in this study for detailed analysis. To compare inter-annual variability in ORAS4, recent well observed ocean data, ARGO gridded data from 2005 to May 2018 is used in this study. ARGO has a good global coverage having around 3° resolution (e.g. Roemmich et al. 1998; Roemmich and Gilson 2009, 2011). All datasets are re-gridded to 1° resolution and anomalies are calculated using 1958–2017 (for ERA data), 1958–2016 (for ORAS4 data) base period climatology and for ARGO the base period for climatology is 2005–2017.

The analysis by Sayantani and Gnanaseelan (2015) was based on SODA reanalysis and the study period was restricted up to 2007 only. However, in the recent years, especially after 2005 (the ARGO era), the subsurface observations have improved drastically especially over the TIO. So in this study ORAS4 data is used in addition to ARGO data and CFSv2 simulations and the analysis is carried out for the period up to 2017, the inclusion of additional well observed period increases the clarity of our conclusions.

The empirical orthogonal function (EOF) analysis is carried out to find the leading modes of variability. The EOFs are calculated using de-trended 100 m depth temperature data. The composite analysis is carried out to understand the mechanism behind the leading mode of variability. Years with the first principal component (PC1) greater than 1 are selected for the composite analysis. Year 0 represents the PC1 peak year and Year 1 represents the following year. Student's two tailed t test is used in this study to examine the significance. Correlation and regression analysis is carried out to understand subsurface–surface interaction in TIO. Years with standardized Niño 3.4 SST anomalies averaged for November–January greater than 0.5 are selected as El Niño years. Years with normalized Dipole Mode Index (DMI) averaged for September–November greater than 1 are selected as IOD years. The IOD and El Niño years are consistent with Gnanaseelan et al. (2012). The Ekman

transport and Ekman pumping velocities are calculated using the following formula:

$$\text{Meridional Ekman transport} = \frac{-\tau_x}{\rho f} \quad (1)$$

Ekman pumping velocity is calculated as in Yokoi et al. (2008)

$$\text{Ekman pumping velocity} = \frac{\text{wind stress curl}}{\rho f} + \frac{\beta \tau_x}{\rho f^2} \quad (2)$$

where wind stress curl = $\frac{\partial \tau_y}{\partial x} - \frac{\partial \tau_x}{\partial y}$ and ρ is the density of ocean water and f is the Coriolis parameter.

3 Subsurface mode in CFSv2

CFSv2 is the coupled ocean atmosphere model used for the operational dynamical forecasts in India from extended range to seasonal scale and to climate change studies. CFSv2 displays surface cold bias and subsurface warm bias in TIO and deeper and warmer thermocline (Achuthavarier et al. 2012; De et al. 2016; Chowdary et al. 2016b, c). The interannual variability in ORAS4 is similar to that of ARGO data. To examine whether the observed north–south mode (Sayantani and Gnanaseelan 2015) is captured by CFSv2, as it has strong influence on the thermocline SST coupling, we have first looked at the leading mode of variability at 100 m temperature for September–November (SON, Fig. 1). It is clear from the leading mode of variability (EOF) that CFSv2 captures the observed subsurface temperature variability well during SON. The northern cooling is seen around the eastern equatorial Indian Ocean (EIO) mostly east of 80°E. It extends up to 8°–10° latitude on both sides of the equator in the east of 80°E (Fig. 1a). The latitudinal variation of the cooling is less in CFSv2 compared to ORAS4 and ARGO. Strong warming is apparent around 10°S and west of 90°E. It extends up to western TIO but stronger signals are seen between 65°E–90°E and 15°S–5°S. Despite having weaker latitudinal variation and more than observed westward extension of southern pole, CFSv2 is able to represent these patterns well during SON. The leading principal components (PC1) of ORAS4 and CFSv2 are shown in Fig. 1c, d.

The seasonal composites of significant 100 m temperature (shaded) and d20 anomalies (contours) for seasons SON(0), DJF(0) and MAM(1) are shown in Fig. 2a–f. The model does a good job in representing the observed pattern of both southern (south-western) warming and northern (north-eastern) cooling of SON (0) (Fig. 2a, d). However it fails to capture the intensification of the mode in DJF(0)

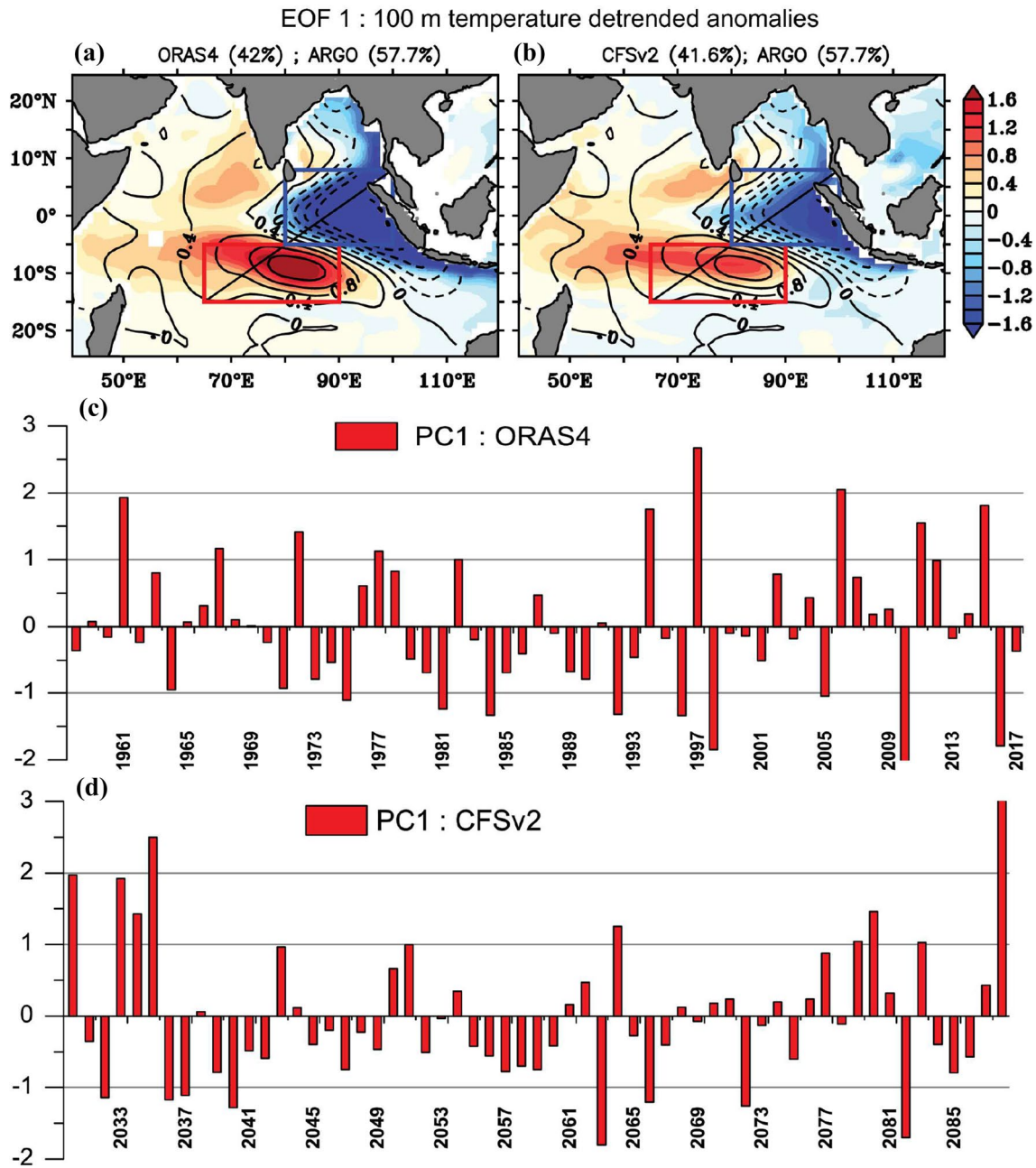


Fig. 1 EOF1 of 100 m temperature de-trended anomalies ($^{\circ}\text{C}$) for September–November **a** ORAS4 (shaded), ARGO (contours) and **b** CFSv2 (shaded), ARGO (contours); PC1 of 100 m temperature de-trended anomalies ($^{\circ}\text{C}$) for September–November **c** ORAS4 and **d** CFSv2

(Fig. 2b, e), instead the southern warming weakens and the northern cooling almost disappears in DJF(0). Further during MAM(1) very weak signals are seen in the model (Fig. 2c, f). The d20 anomalies and 100 m temperature anomalies show similar patterns of evolution both in the observations and model.

Figure 2g–i shows the evolution of vertical structure of this mode in ORAS4 and CFSv2 along the line of dominance shown in Fig. 1a. The line is drawn from (65°E , 15°S) to (100°E , 8°N) joining the southwest corner of the southern box to northeast corner of the northern box

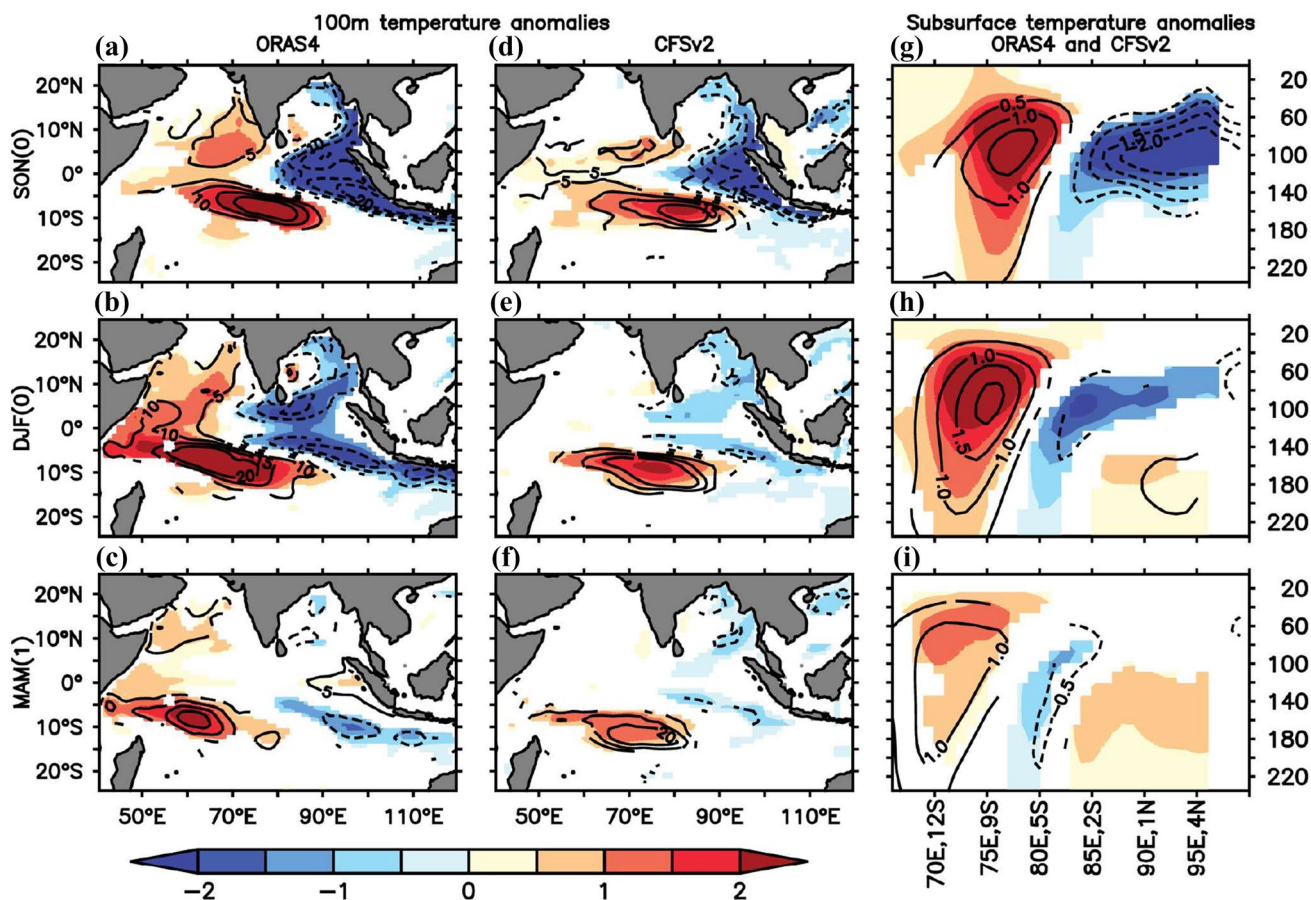


Fig. 2 Composite of 100 m temperature anomalies (shaded, °C) and d20 anomalies (contours, m) for **a–c** ORAS4 and **d–f** CFSv2; **g–i** Composite of subsurface temperature anomalies (°C) along line from

(65°E, 15°S) to (100°E, 8°N) shown in Fig. 1a. ORAS4 (shaded) and CFSv2 (contours) at 90% confidence level for **a, d, g** SON(0), **b, e, h** DJF(0), **c, f, i** MAM(1)

shown in Fig. 1a, which represents the actual direction of the so called north–south mode. The composite of subsurface temperature anomalies over this line for the three seasons [SON(0), DJF(0) and MAM(1)] are shown in Fig. 2g–i. It is clear from the figure that the subsurface mode persists up to MAM(1) (Fig. 2g–i). However the northern cooling weakens or disappears by DJF(0) in CFSv2 (Fig. 2h). It is also clear that the weakening of the subsurface mode in CFSv2 is caused by rapid decay of northern signals.

The cooling along the east equatorial region and warming around 10°S are two highlighting aspects of this tilted north–south dipole. To understand the four dimensional structure of variability over these regions in detail, the monthly evolutions of the subsurface temperature (depth–longitude) anomalies averaged over 5°S–5°N and at 10°S in ORAS4 and CFSv2 are shown

in Fig. 3. Strongest cooling (warming) over eastern (western) equatorial IO is seen in Nov(0) in ORAS4 and CFSv2 (Fig. 3c). It is evident that the east–west subsurface variability along the equatorial IO is strongest in Nov(0) (Fig. 3c), thereafter the eastern cooling weakens in both ORAS4 and CFSv2, however the weakening is more rapid in CFSv2 (Fig. 3e, f). On the other hand the western warming along 10°S intensifies from Nov(0) onwards (Fig. 3i–k) both in the reanalysis and model. The difference is that the peak warm anomalies are found at around 100 m in the reanalysis where as it is at about 150 m in the model. This discrepancy in the model could be due to the deeper than observed thermocline in the model. There is upward propagation of warm anomalies in the central to western region in ORAS4, which could strengthen the subsurface surface interaction and in turn amplify the air–sea interaction. Such upward

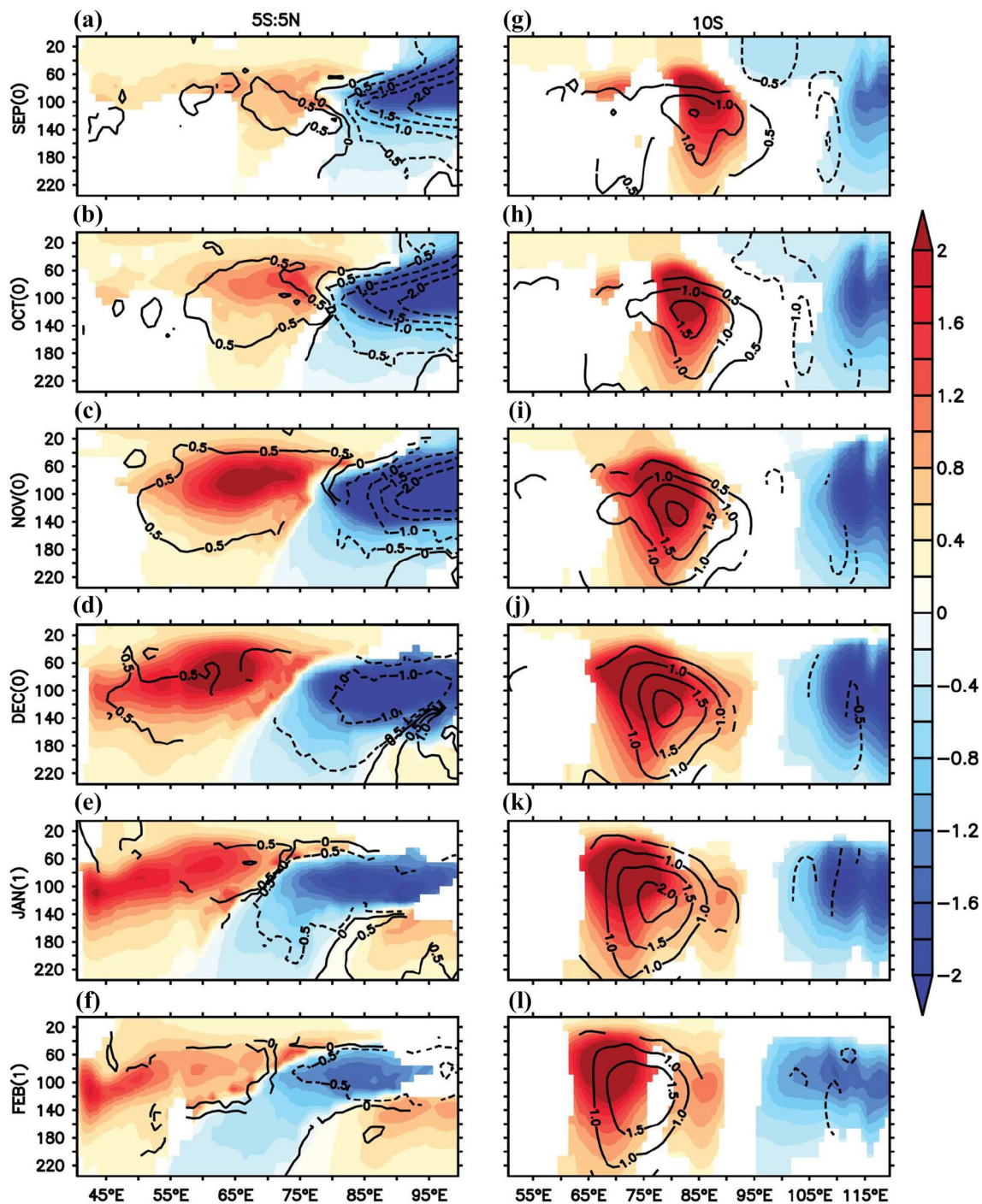
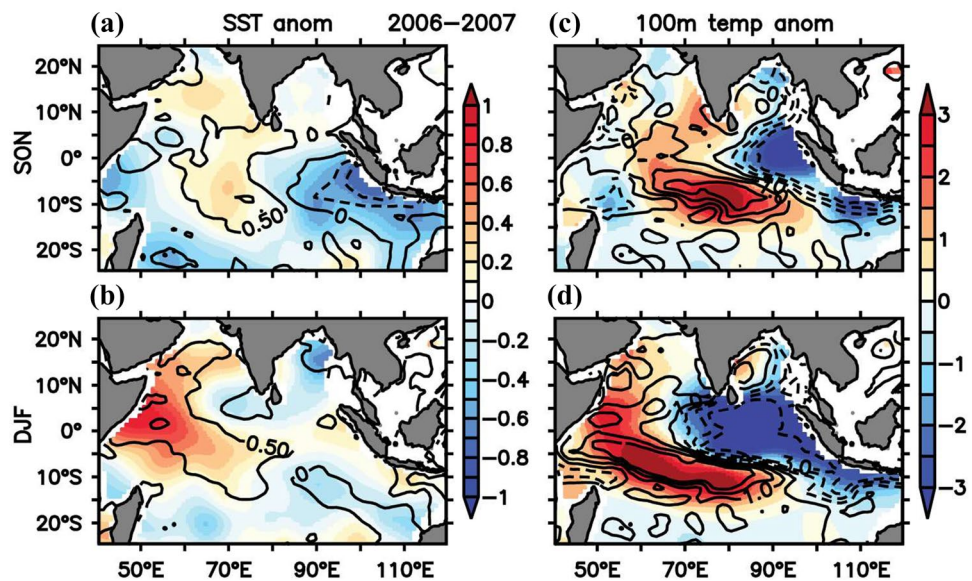


Fig. 3 Composite of subsurface temperature anomalies ($^{\circ}\text{C}$) **a–f** averaged over 5°S – 5°N and **g–l** at 10°S . ORAS4 (shaded) and CFSv2 (contours) at 90% confidence level for **a, g** Sep(0), **b, h** Oct(0), **c, i** Nov(0), **d, j** Dec(0), **e, k** Jan(1), **f, l** Feb(1)

propagation of warm anomalies is underestimated in the model leading to the suppression of thermocline SST coupling. Thus overall CFSv2 captures the subsurface

mode during SON, but the magnitude weakens in the subsequent seasons and the spatial extent is limited compared to the observations. In fact, the model could not

Fig. 4 **a, b** SST anomalies ($^{\circ}\text{C}$) and **c, d** 100 m temperature anomalies ($^{\circ}\text{C}$) for **a, c** SON and **b, d** DJF in 2006–2007 using ARGO (shaded) and ORAS4 (contours)



maintain this mode beyond SON(0) mostly because of its inability to sustain the northern cooling. The year 2006 turns out to be a strong subsurface mode year (Fig. 1c) in the recent well observed period, which is also an El Niño–IOD co-occurrence year (e.g. Gnanaseelan et al. 2012). Thus surface and subsurface evolution during 2006–2007 is examined as a case study. Figure 4 shows the SST anomalies and 100 m temperature anomalies during SON and DJF of 2006–2007 using ARGO observations and ORAS4. It is clear that the TIO SST shows east west dipole in SON, but the subsurface anomalies strengthen in DJF with more of a north–south structure rather than the traditional east–west structure supporting the existence of the dominant north–south mode as reported by Sayantani and Gnanaseelan (2015).

4 Mechanism behind the early termination of the subsurface mode in CFSv2

The early termination of the subsurface mode in CFSv2 is characterized by weakening southern warming with less longitudinal coverage and rapid decay of northern cooling in December itself. The mechanisms associated with these two patterns are different. Oceanic Rossby waves are mainly contributing to the STIO variability, whereas equatorial anomalies are driven by Kelvin wave dynamics. The anomalous equatorial easterlies forced by the off-equatorial anticyclones and the associated wind stress curl are found to be the primary forcing mechanism for the

generation and maintenance of the subsurface mode. The wind stress curl and the associated Ekman pumping are found to contribute primarily to the generation and propagation of Rossby waves in STIO (Masumoto and Meyers 1998; Gnanaseelan and Vaid 2010). The surface easterly anomalies at the equator generate poleward mass transport, and the associated divergence at the equator generates upwelling Kelvin waves. These waves move eastward and cool the eastern equatorial IO. The poleward Ekman transport helps in deepening the thermocline generating downwelling Rossby waves at the convergence latitude. The Ekman transport and the downwelling favourable wind stress curl induce the off-equatorial Rossby waves. The composite of wind stress and wind stress curl anomalies are shown from JJA(0) to DJF(0) in Fig. 5. The southeasterly wind anomalies are seen in JJA(0) (Fig. 5a, d) in both the observations and model. But these anomalies are confined to the eastern IO in the model with weak equatorial easterlies than in the observations. These easterlies get strengthened in SON(0) (Fig. 5b) and weakened by DJF(0) (Fig. 5c). The anomalous positive wind stress curl around 10°S is weak in JJA(0) (Fig. 5a) but gets strengthened in SON(0) (Fig. 5b) spanning most of the STIO between 5°S and 15°S. On the other hand, the curl weakens in DJF(0) (Fig. 5c). The model also exhibits surface easterlies in SON(0) (Fig. 5e). But the positive wind stress curl anomalies over STIO are weaker and confined to the east of 70°E with less latitudinal spread. These wind stress curl anomalies get weakened in DJF(0) (Fig. 5f). This in turn has modulated (or weakened) the downwelling Rossby waves

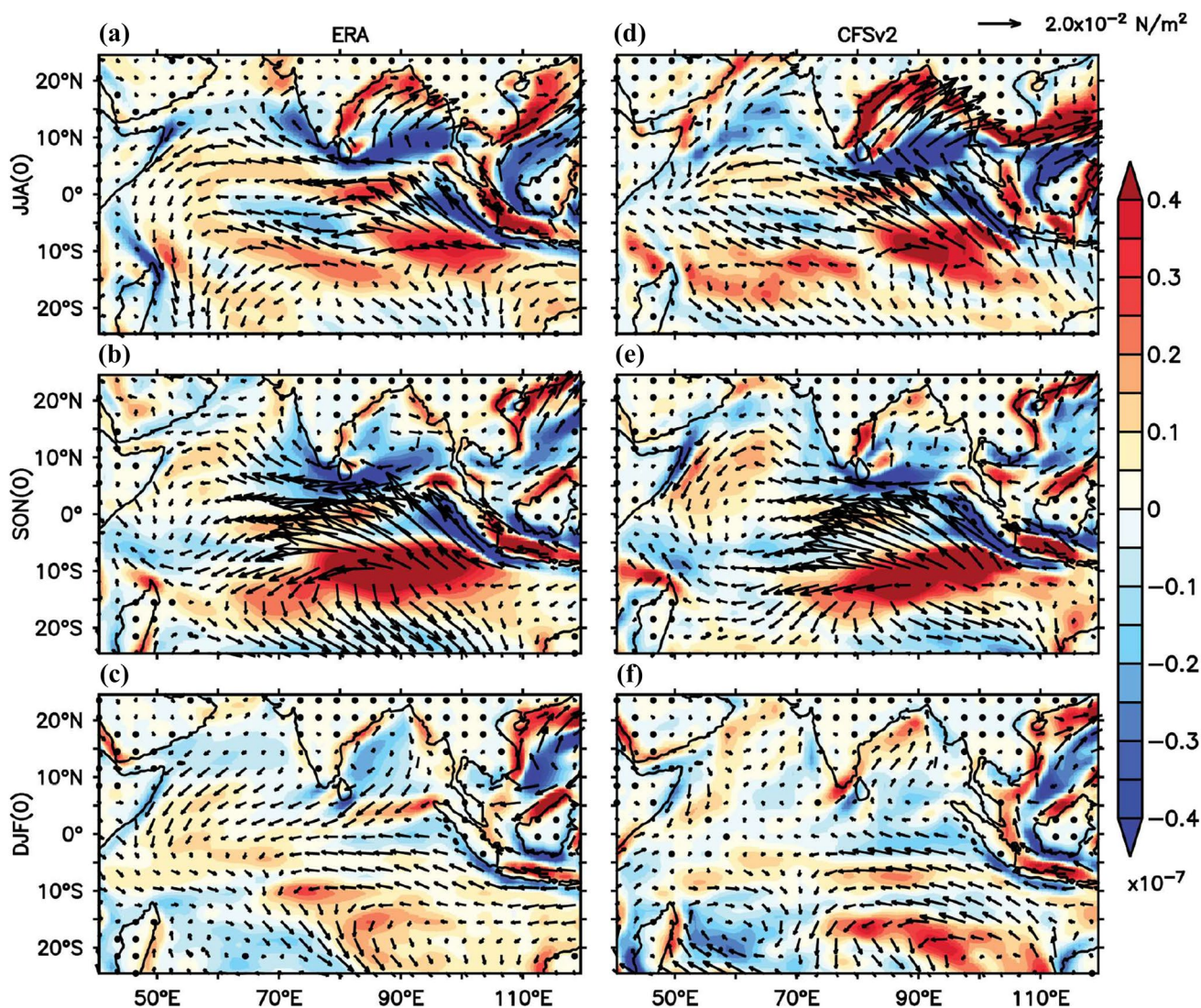


Fig. 5 Composite of wind stress curl anomalies (shaded, $\times 10^{-7} \text{ N/m}^3$) and wind stress anomalies (vectors, $\times 10^{-2} \text{ N/m}^2$) at 1000 hPa for **a–c** ERA and **d–f** CFSv2 for **a, d** JJA(0), **b, e** SON(0), **c, f** DJF(0)

resulting in early weakening of southern warming especially in the west. The anomalous Ekman pumping velocity and Ekman transport are shown in Fig. 6. The downward Ekman pumping around 10°S is not well captured in CFSv2. The easterly (westerly) anomalies in SON(0) are seen north (south) of 10°S with peak around equator (20°S) in observations (Fig. 5b). This supports southward (northward) transport from the region north (south) of 10°S supporting strong surface convergence at 10°S (Fig. 6b) strengthening the downwelling Rossby waves. These patterns continue to persist in DJF(0) (Fig. 6c) as well. In contrast, the model winds (near 10°S) are similar

to observations only east of 75°E (Fig. 5). Therefore the integration of these forcing along the longitude is primarily responsible for the observed stronger signals during DJF(0). These are consistent with the limited westward extension of forcing and subsurface warming etc. in the model. In fact, in DJF(0), anomalous cyclonic circulation is seen in SWTIO (between 10°S – 20°S and 50°E – 70°E) in the model (Fig. 5f) unlike in the observations (Fig. 5c). The associated negative wind stress curl anomalies further weaken the downwelling Rossby waves and limit their westward propagation in the model. The differences

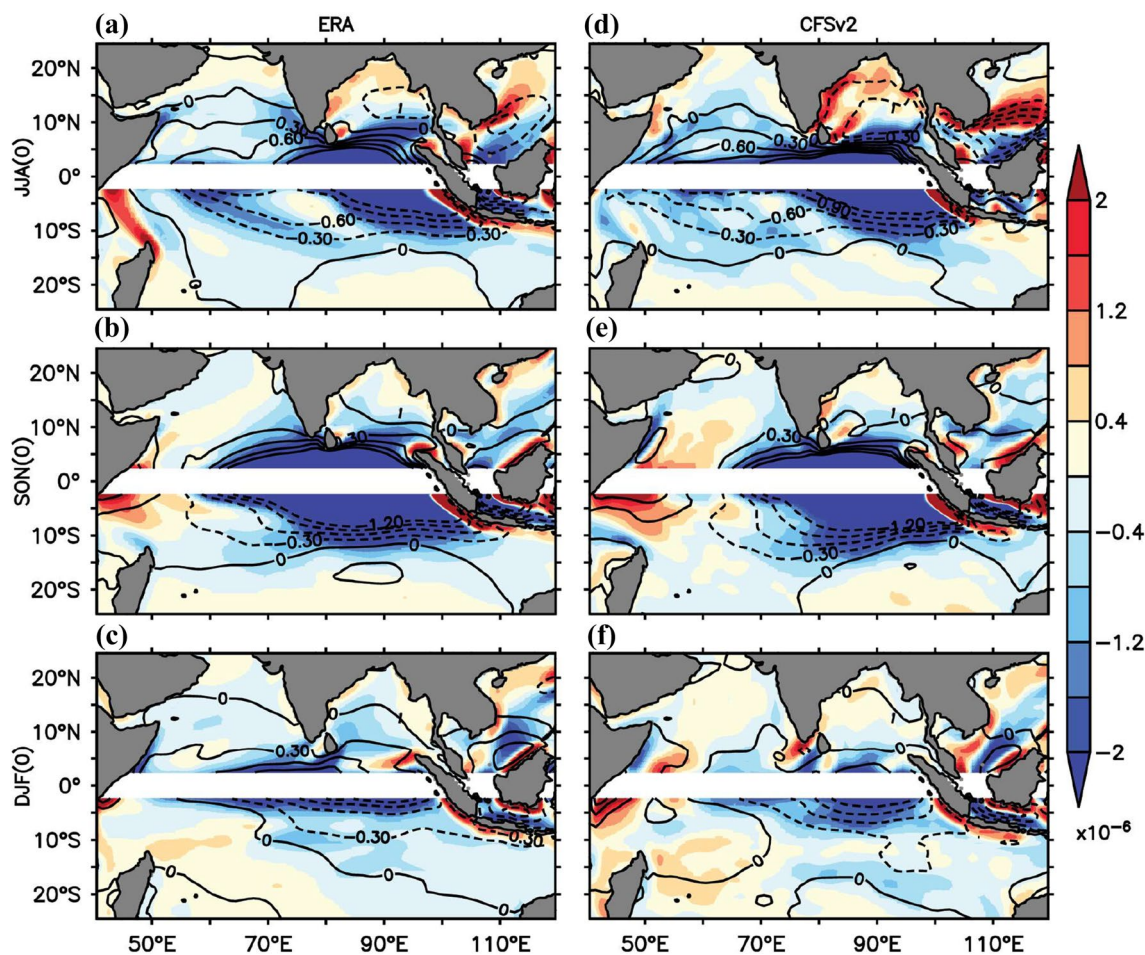


Fig. 6 Composite of Ekman pumping velocity (shaded, $\times 10^{-6}$ m/s) and Ekman meridional transport (contours, m^2/s) at 1000 hPa for **a–c** ERA and **d–f** CFSv2 free run for **a, d** JJA(0), **b, e** SON(0), **c, f** DJF(0)

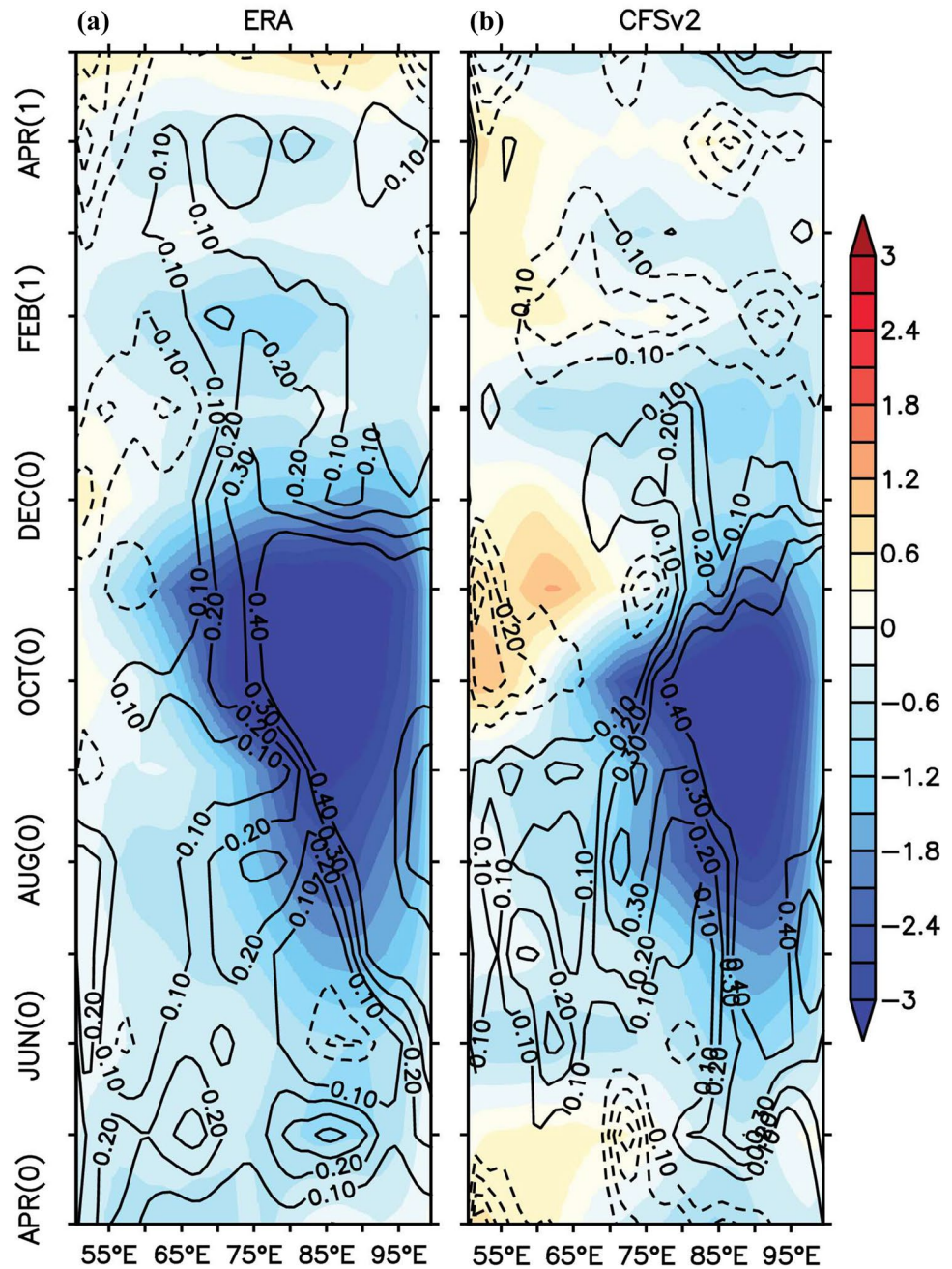
in the wind stress curl anomalies at $10^\circ S$ can be clearly seen from Fig. 7. Model exhibits anomalous negative wind stress curl after December (0) supporting the weakening of downwelling signals over that region.

Composite evolution of zonal wind anomalies over the equator are shown in Fig. 7. It is found that the easterly wind anomalies along the equator are weaker in the model (Fig. 7b) as compared to the observations (Fig. 7a). This underestimation of anomalous easterlies along the equator suppresses the upwelling Kelvin waves in the model. This further affects the representation of cooling in the eastern equatorial IO in the model. Also eastward propagating westerly wind stress anomalies are seen in the western IO from Oct(0) in the model (Fig. 7b). Westerly wind anomalies in the model are favourable for generating downwelling Kelvin waves. As discussed above, the

Rossby waves on the other hand had limited westward propagation and so could not reach SWTIO in the model. Hence warming in the west is locally generated, mainly due to the westerly wind anomalies over that region, as seen in Fig. 7. In addition to that the positive wind stress curl anomalies at $10^\circ S$ are seen in ORAS4 up to April (1) but are seen only up to December (0) in CFSv2. Thus downwelling related to wind stress curl is weak in CFSv2 after December (0).

To understand the large-scale circulation patterns in both the observations and model, we have carried out further analysis. The divergent component of wind at 1000 hPa is shown in Fig. 8. The divergence in south eastern IO is well captured by the model in JJA(0) (Fig. 8a, d) and SON(0) (Fig. 8b, e). But the convergence over the equatorial Pacific is very weak in CFSv2 which weakens

Fig. 7 Composite of time evolution of zonal wind anomalies (m/s) at 1000 hPa at equator and wind stress curl anomalies ($\times 10^{-7} \text{ N/m}^3$) at 1000 hPa at 10°S for **a** ERA and **b** CFSv2 from Apr(0) to May(1)



the Walker cell circulation as well (figure not shown). In DJF(0) divergence in the model is weaker than the observations with southward shift in the divergent center (Fig. 8c, f). To trace back the origin of the differences in wind anomalies in the observations and model, we have analysed the mslp anomalies (Fig. 9). In JJA(0), the model shows positive mslp anomalies over most of the IO basin with positive center between 10°S and 20°S in south-eastern TIO (Fig. 9d). But observations show positive mslp

anomalies over Australia and negative mslp anomalies over western IO (Fig. 9a). This supports strong southeasterly wind anomalies extending up to 60°E from eastern TIO in the observations, which are not well represented in the model (Fig. 5). In SON(0), two positive mslp centers are seen in the observations as Gill's response (Gill 1980) to the eastern cooling, one over the south-eastern TIO and the other over the Bay of Bengal (BoB) (Fig. 9b). Also negative mslp anomalies are seen in WIO (west of

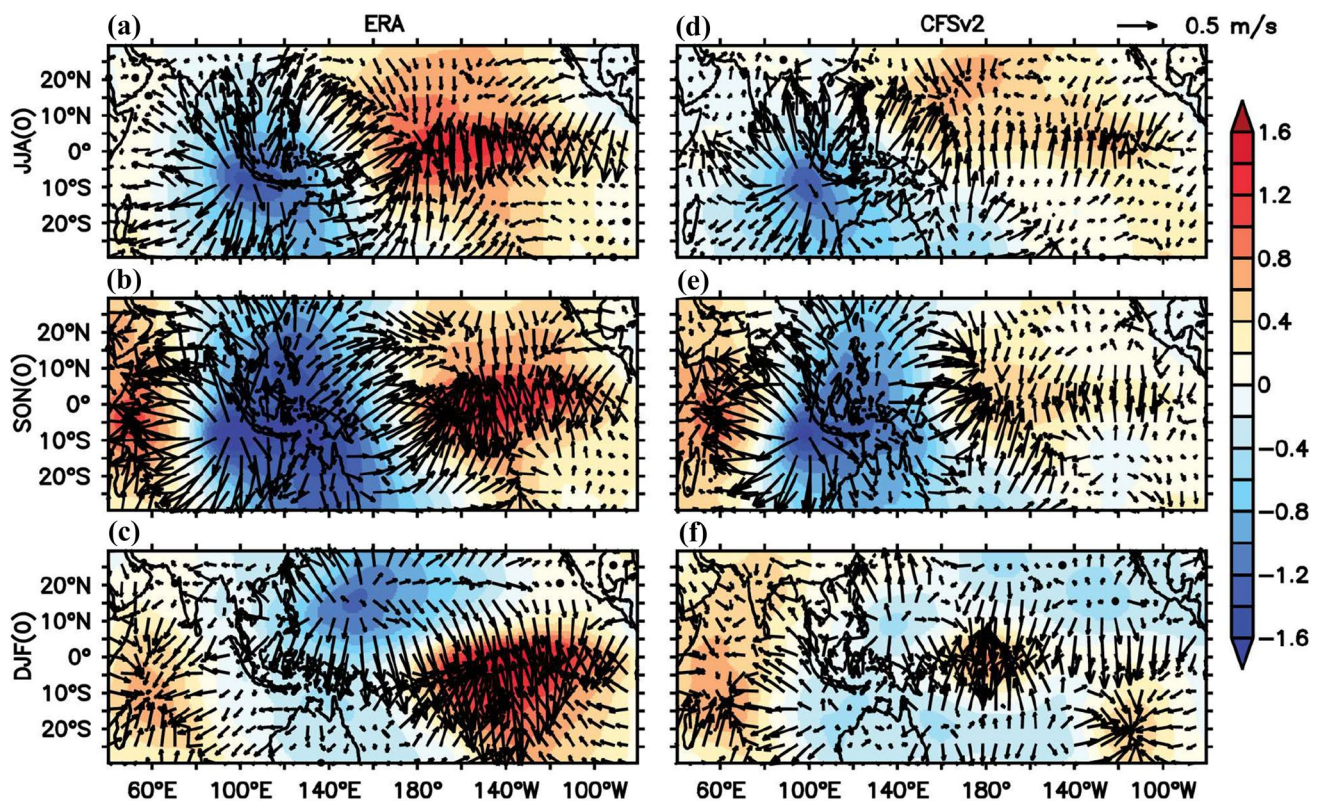


Fig. 8 Composite of velocity potential (shaded, m^2/s) and divergent component of wind anomalies (vectors, m/s) at 1000 hPa for **a–c** ERA and **d–f** CFSv2 for **a, d** JJA(0), **b, e** SON(0), **c, f** DJF(0)

60°E). This supports strong surface easterly anomalies over the equator. The model does not show the high pressure center over the BoB during SON(0) (Fig. 9e). The negative anomalies in the west also extended up to 75°E in the model. This has resulted in the eastward shift of the convergence centre. Large differences in the observations and model can be seen in DJF (0) as well. During DJF two positive mslp anomaly centers are seen over south-eastern IO and north-west Pacific (NWP) region in the observations (Fig. 9c, f). The NWP high pressure centre is also not well represented in the model. On the other hand the negative mslp anomalies over the western IO persisted in DJF(0) in the model.

Previous studies (Wang et al. 2003; Xiang et al. 2011) discussed the role of mean vertical shear and associated low level anticyclones in maintaining the zonal equatorial easterlies in the IO. These anticyclones are responsible for the anomalous equatorial surface easterly anomalies. The STIO anticyclone is seen in both the observations and model in all the seasons in the anomalous rotational

component of wind (Fig. 10). But in SON(0) and DJF (0) the STIO anticyclone is restricted to east of 70°E. On the other hand, the northern anticyclone over the BoB is very weak in the model while the observed anticyclone is wide spread covering the whole BoB, southern Indian land region and some parts of eastern Arabian Sea. However the anticyclone in the model is confined only over the BoB in all the seasons. The intensity is also very weak in the model compared to that of the observations. The anticyclonic circulation over the NWP region in DJF (0) is also weaker than observed. The mean vertical wind shear plays an important role in the formation of these anticyclones (Wang et al. 2003). The mean vertical shear is also weaker in the model compared to the observations (Fig. 9). Clear differences can be seen over the southwest Pacific in DJF(0). ORAS4 shows strong cyclonic circulation whereas CFSv2 displays anticyclonic circulation over the southwest tropical Pacific. The inability of the model in capturing the anticyclonic circulations correctly (mainly the one in the northern hemisphere) turns out to

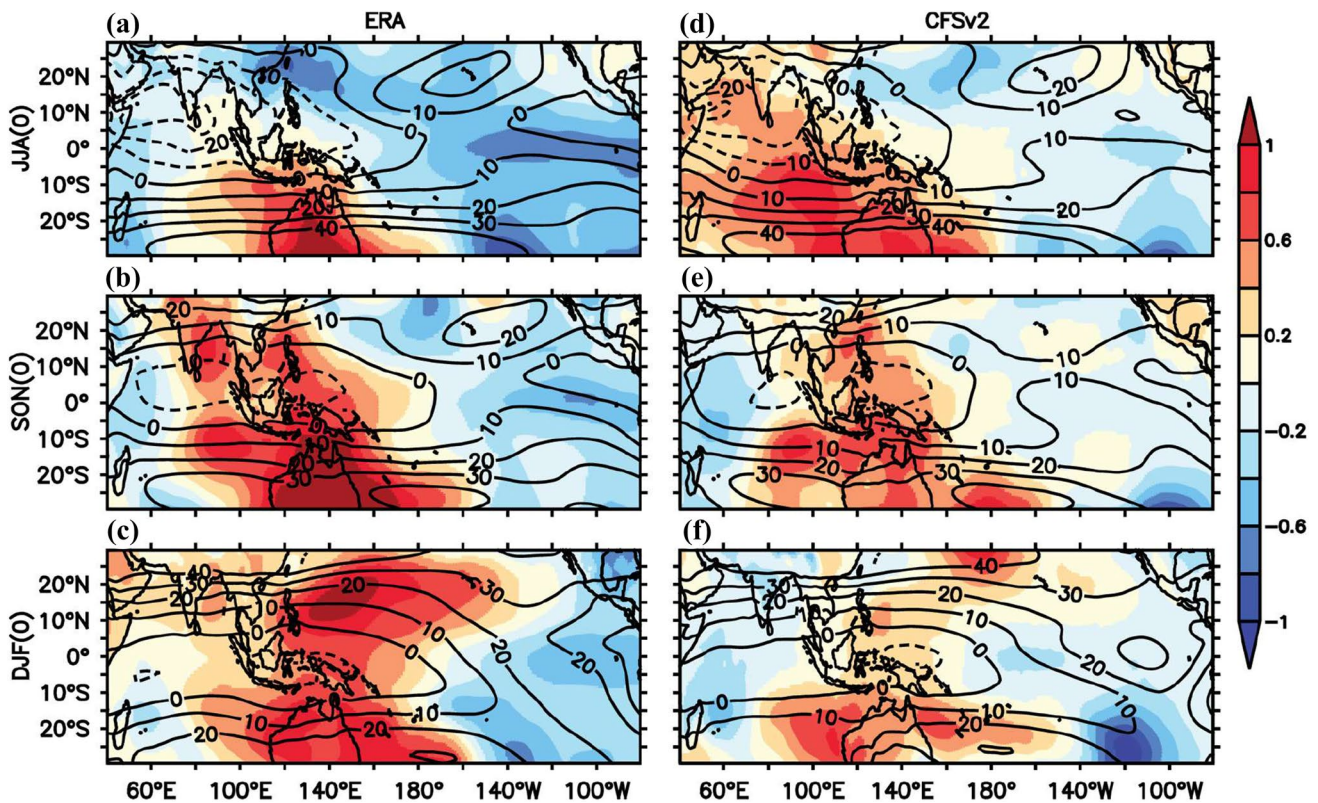


Fig. 9 Composite of mean sea level pressure anomalies (hPa) (shaded) and mean vertical shear (200–850 hPa) of zonal wind (m/s) (contours) for a–c ERA and d–f CFSv2 for a, d JJA(0), b, e SON(0), c, f DJF(0)

be the prime cause of the misrepresentation of the surface zonal wind anomalies. It is important to note that the early termination of north–south mode in CFSv2 is closely associated with the misrepresentation of wind anomalies and the associated ocean dynamics.

5 Association of the subsurface mode with the Indo-Pacific SST climate modes

Sayantani and Gnanaseelan (2015) reported that the north–south mode peaks in December–February (DJF), since it is not only driven by the internal forcing over TIO but is also forced externally from Pacific. They reported that the maintenance of TIO subsurface mode is closely associated with the evolution of major climate modes such as IOD and El Niño. We have first examined whether the climate modes such as IOD and El Niño are evolved properly with observed strength, frequency and seasonal cycle. The standard deviation of Niño 3.4 is

slightly underestimated in the model, whereas the standard deviation of DMI is slightly overestimated. However, both of these indices of CFSv2 and ORAS4 were comparable. Since the early termination of subsurface mode in CFSv2 is due to the misrepresentation of wind anomalies over the Indo-Pacific region, it is necessary to evaluate the performance of CFSv2 in simulating IOD and El Niño years. Figure 11 shows the composites of 100 m temperature anomalies for Pure IOD, Pure El Niño and IOD, El Niño co-occurrence years for the three seasons [SON(0), DJF(0), MAM(1)]. ORAS4 data has 4 pure IOD, 14 pure El Niño and 6 El Niño–IOD, co-occurrence years while CFSv2 has 4 pure IOD, 15 El Niño and 2 El Niño–IOD co-occurrence years. It is clear from Fig. 11 that the subsurface dipole is not well captured during the El Niño–IOD co-occurrence years in CFSv2. The reanalysis data shows the maintenance and strengthening of subsurface dipole in DJF(0) during El Niño–IOD co-occurrence years but CFSv2 instead shows weakening of dipole. Thus it is necessary to study the IOD and El

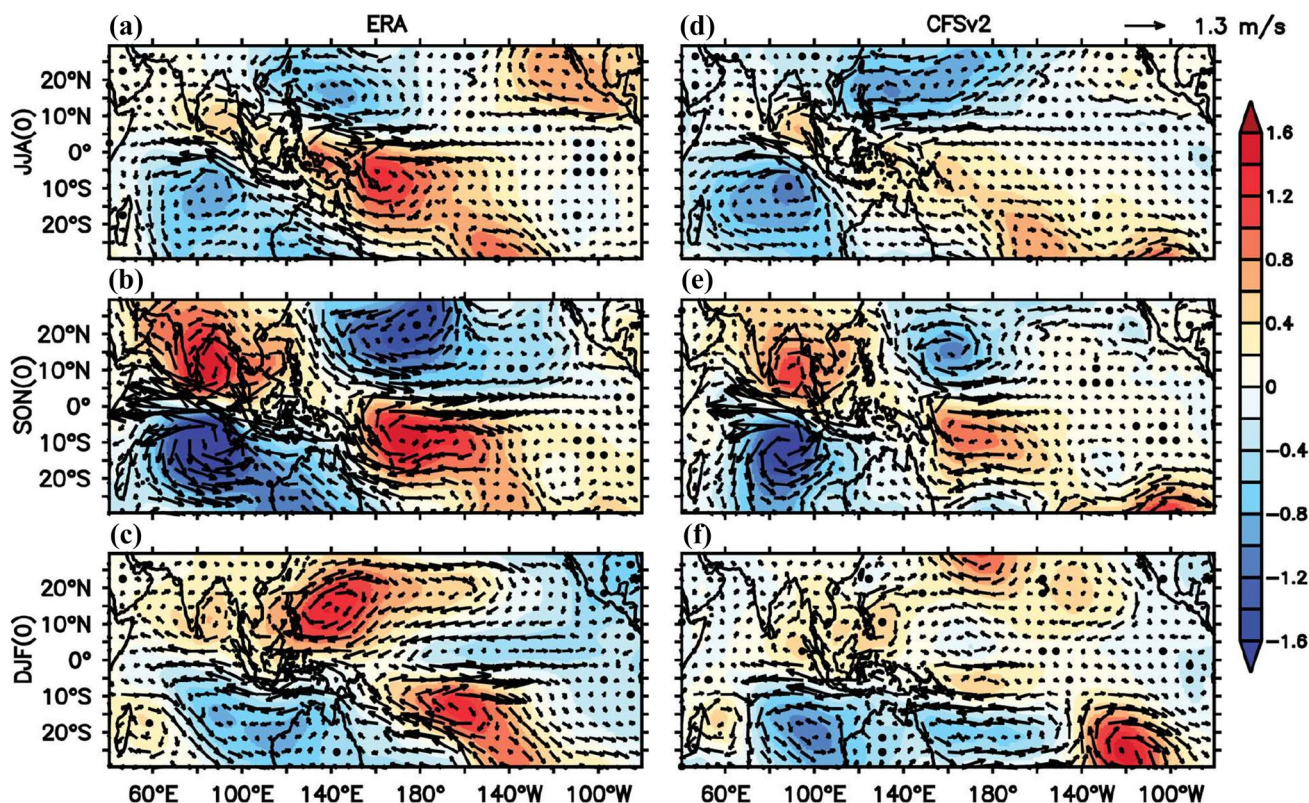


Fig. 10 Composite of stream function (shaded, s^{-1}) and rotational component of wind anomalies (vectors, m/s) at 1000 hPa for **a–c** ERA and **d–f** CFSv2 for **a, d** JJA(0), **b, e** SON(0), **c, f** DJF(0)

Niño evolution in CFSv2. To understand this further, the composites of Niño 3.4 and DMI time series are plotted in Fig. 12. It can be seen that the differences in the evolution of Niño 3.4 SST anomalies between ORAS4 and CFSv2 are more during the IOD, El Niño co-occurrence years. Chowdary et al. (2016a) showed a 2 month delay in the decay of El Niño in CFSv2. We report that this delay however is found mainly during the El Niño, IOD co-occurrence years in CFSv2 (Fig. 12a) and not during the pure El Niño years. This strongly suggests the role of evolution of TIO temperature and the associated air–sea interaction in the representation of El Niño cycle (especially the decay phase) in the model. Compared to El Niño evolution, IOD evolution is well captured in CFSv2 (Fig. 12b), but clear differences are seen during the El Niño, IOD co-occurrence years. We have also examined whether our conclusions are biased by few strong events such as that of 1997, and to our surprise, it is found that the conclusions remain same without the strong events as well (figure not shown). Composite of SST anomalies

and wind anomalies at 1000 hPa for pure IOD, pure El Niño and El Niño, IOD co-occurrence years are shown in Fig. 13. IOD related east–west dipole in SON and El Niño related basin wide warming in DJF are comparable in both ORAS4 and CFSv2. But during co-occurrence years clear differences are evident during DJF. In DJF, ORAS4 displays basin wide warming signals but CFSv2 has weak cooling over south eastern IO. This opens up another potential area for immediate attention.

6 Role of subsurface mode on TIO basin wide warming associated with ENSO

Figure 14a shows the time series of composite TIO SST anomalies ($40^{\circ}\text{E}:100^{\circ}\text{E}$, $20^{\circ}\text{S}:20^{\circ}\text{N}$, normalized with respective standard deviation) for El Niño, Pure El Niño and the El Niño, IOD co-occurrence years. Figure 14b shows the composites of TIO SST anomalies for subsurface mode peak, subsurface mode co-occurring with El

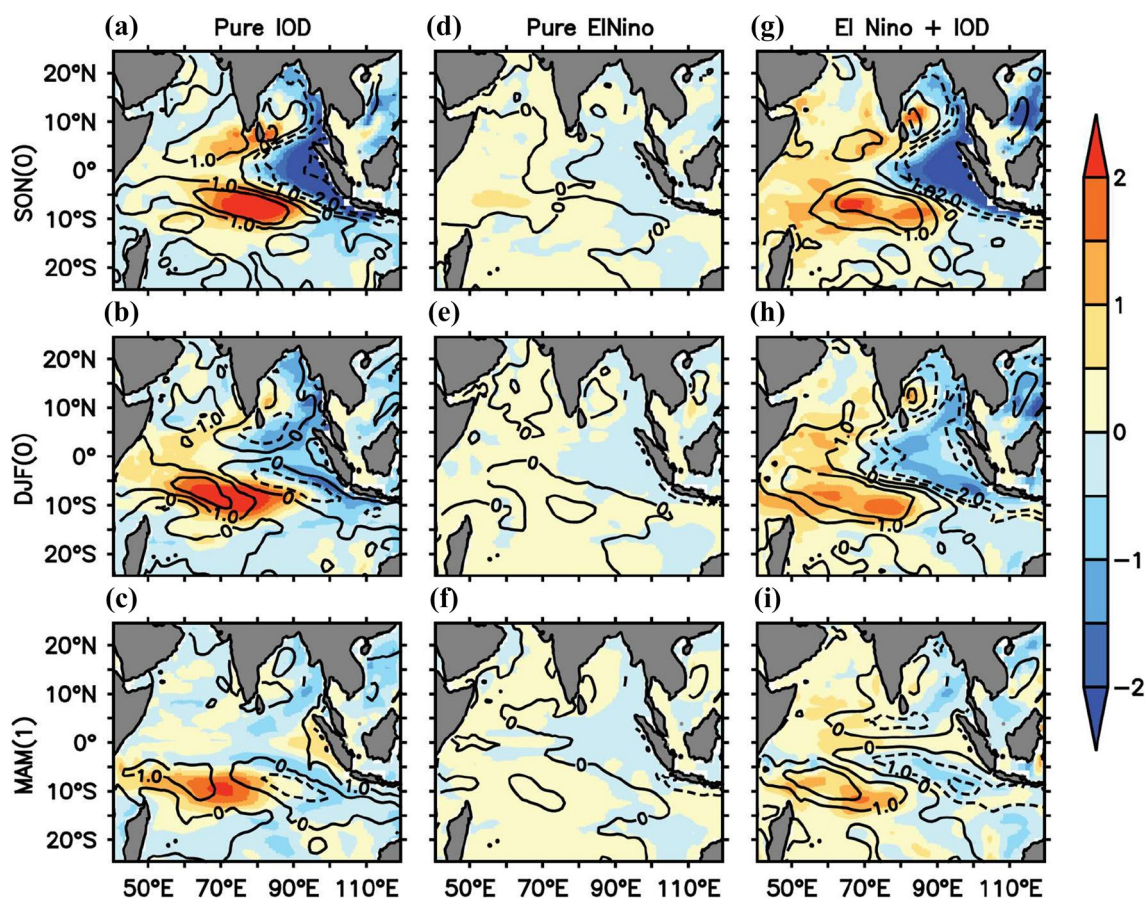
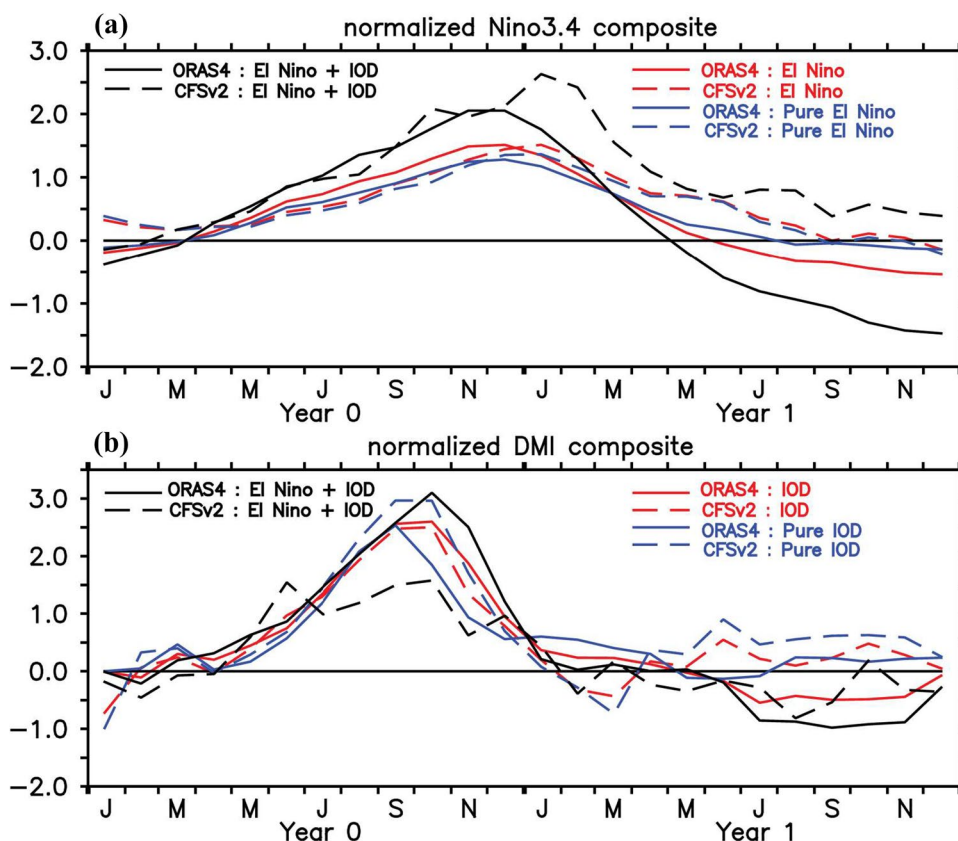


Fig. 11 Composite of 100 m temperature anomalies ($^{\circ}\text{C}$) **a–c** composite of Pure IOD years **d–f** composite of Pure El Niño years, **g–i** composite of El Niño and IOD co-occurrence years, CFSv2 (shaded) and ORAS4 (contours) for **a, d, g** SON(0); **b, e, h** DJF(0) and **c, f, i** MAM(1)

Niño and co-occurring with both El Niño and IOD. Using correlation analysis Chowdary et al. (2016a) reported rapid decay of TIO basin-wide SST warming associated with El Niño in CFSv2. Such rapid decay is seen in the composite of subsurface mode peak co-occurring with both El Niño and IOD (Fig. 14b). However, the evolution of TIO warming in all other composites of CFSv2 is consistent with the observation. It is therefore convincing that this rapid decay in TIO SST warming in CFSv2 is mainly due to the misrepresentation of subsurface variability and associated SST evolution over TIO. The maintenance of subsurface dipole supports the westward propagation of the downwelling off-equatorial signals which in turn supports the surface warming. Changes in the surface warming pattern, due to weak subsurface

anomalies, display strong impact on the regional climate. The representation of subsurface surface interaction over TIO is further studied as it in turn influences the representation of air-sea interaction in the coupled model as reported by Zhou et al. (2018). Figure 15a–d shows the correlation of PC1 with SST anomalies over the Indo-Pacific region. CFSv2 is unable to represent the correlation correctly as seen in ORAS4 during DJF season. To understand the role of subsurface mode on SST anomalies independent of IOD and ENSO, we carried out regression analysis with the SST anomalies (before and after removing the contribution of respective climate modes). The regression coefficient and the composites are shown in Fig. 15e–h. SST anomalies regressed against PC1 and SST anomalies regressed against PC1

Fig. 12 Composite of normalized **a** Niño3.4 and **b** DMI indices for **a** El Niño (red), Pure El Niño (blue) and El Niño, IOD co-occurrence (black) years. **b** IOD (red), Pure IOD (blue) and El Niño, IOD co-occurrence (black) years. Solid line represents ORSA4 and dash line represents CFSv2



after removing IOD and ENSO impact are displayed. The regressed patterns are similar and display positive relation in DJF over the western and southern TIO in ORAS4, but CFSv2 does not show such relation. Thus there is a close association between the early decay of ENSO related TIO basin wide warming and misrepresentation of subsurface mode in TIO in CFSv2. As shown in the previous section, misrepresentation of subsurface mode is due to the incorrect simulation of Indo-Pacific teleconnections. It is clear that the improper Indo-Pacific teleconnections are indirectly affecting the basin wide warming pattern through improper subsurface variability in CFSv2.

7 Summary and discussion

The north–south mode in the TIO subsurface temperature is examined in the coupled model CFSv2. This study shows that the model captures the north–south mode reasonably well compared to the observations during SON. But the mode does not persist for the next two

seasons in the model unlike in the observations. The analysis of four dimensional structure reveals that the northern cooling is terminated by December in the model whereas this cooling persisted for the next two seasons in the observations. The warming in the south is also found weaker in the model than in the observations and is confined to only over central STIO. The mechanism responsible for the early termination of north–south mode in the model is also examined. It is found that the unrealistic representation of wind anomalies over the TIO is primarily responsible for the early termination. The equatorial surface wind anomalies and the associated Ekman transport as well as Ekman pumping are not properly represented in the model. This misrepresentation resulted in the weaker generation and propagation of downwelling Rossby waves in the STIO and affected the southern warming. The equatorial zonal wind anomalies are not well positioned over the equator in DJF (0), thereby inducing weak upwelling Kelvin wave signals in the model. Both the upwelling Kelvin waves over the equator and the upwelling near Sumatra are weaker in the model compared to the observations. This resulted in

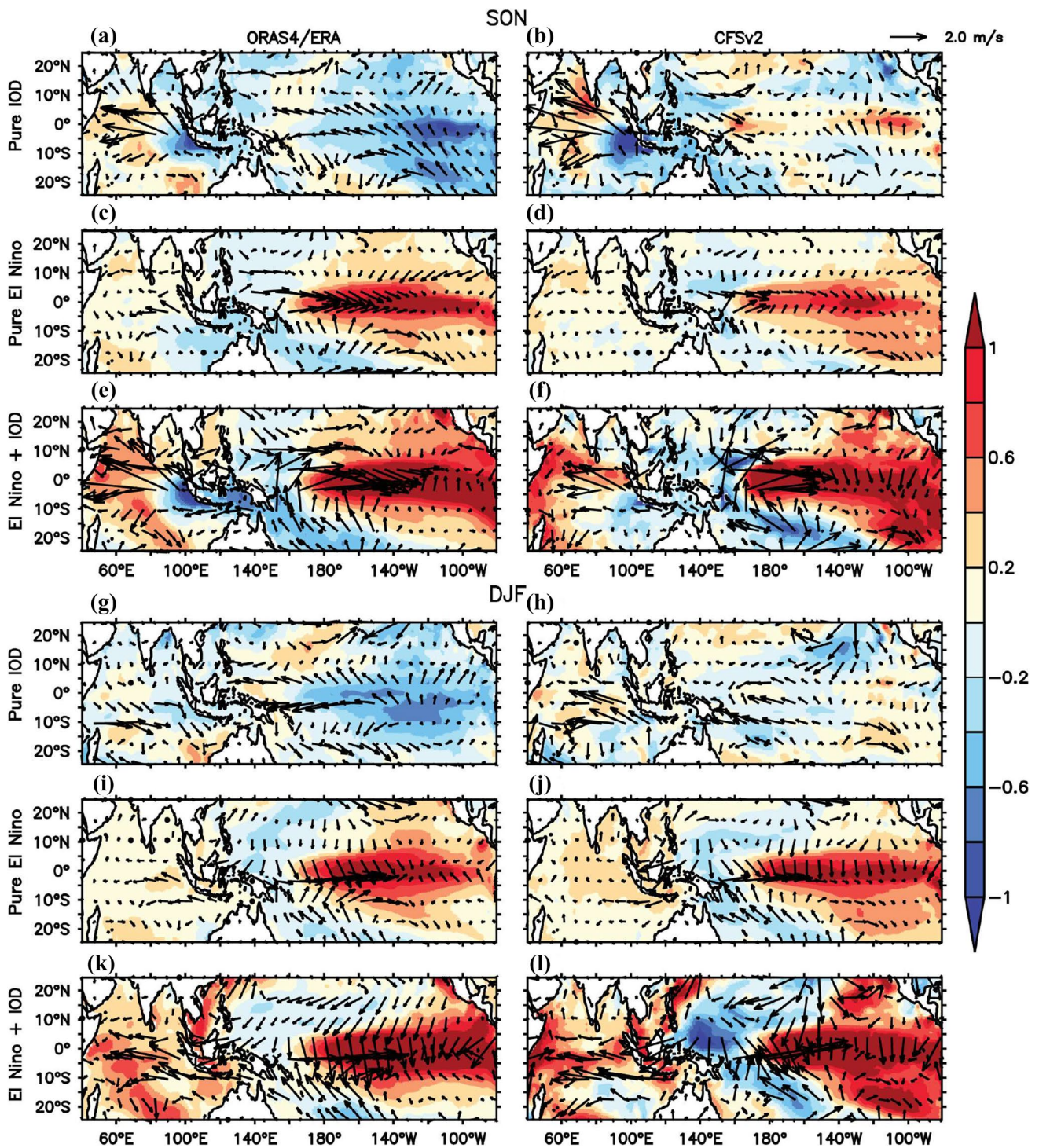
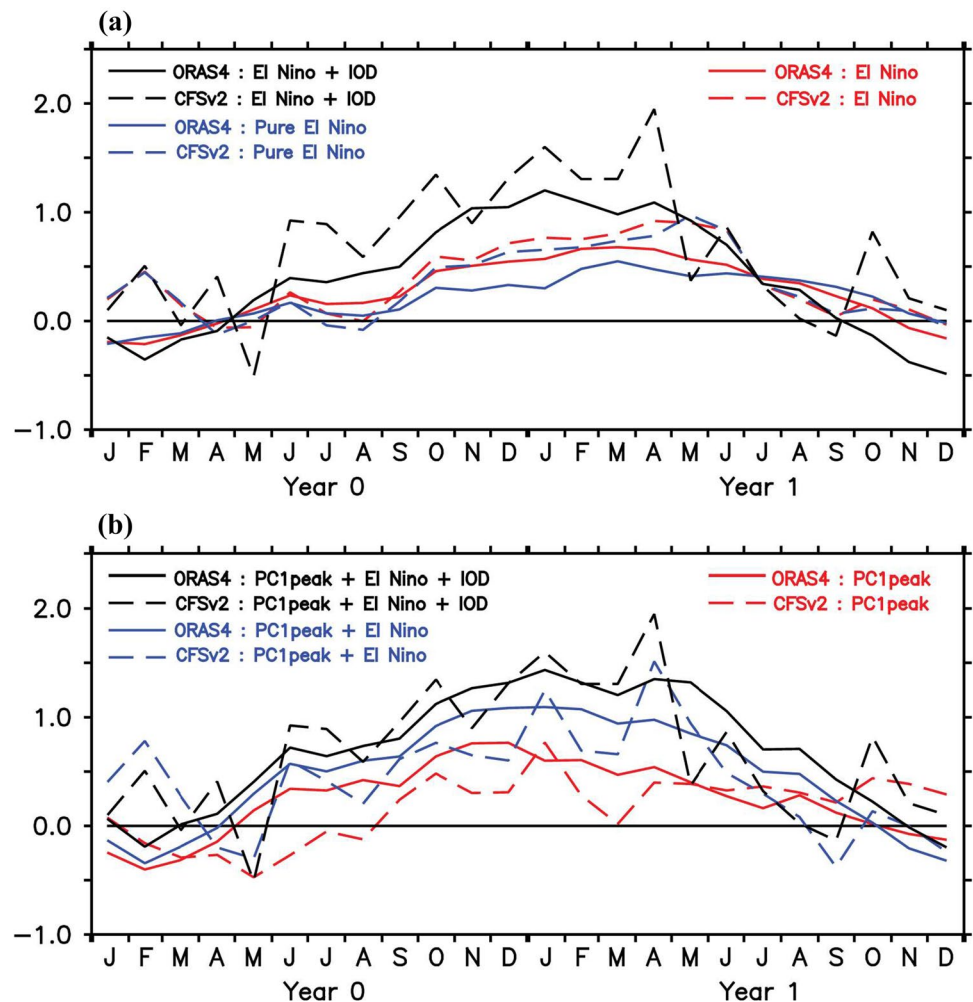


Fig. 13 Composite of SST anomalies ($^{\circ}\text{C}$) and wind anomalies at 1000 hPa (m/s) a, c, e ORAS4/ERA (for SON), g, i, k ORAS4/ERA (for DJF), b, d, f CFSv2 (for SON), h, j, l CFSv2 (for DJF). Compos-

ites of a, b, g, h pure IOD years, c, d, i, j pure El Niño years, e, f, k, l El Niño, IOD co-occurrence years

Fig. 14 Composite of normalized SST anomalies averaged over TIO (40°E–100°E, 20°S–20°N) region **a** El Niño (red), Pure El Niño (blue) and El Niño, IOD co-occurrence (black) years. **b** PC1 peak years (red), PC1 peak, El Niño co-occurrence years (blue) and PC1 peak, El Niño, IOD co-occurrence (black) years. Solid line represents ORAS4 and dash line represents CFSv2



the termination of cooling during DJF(0) in the model, instead of the observed strengthening. The observations show that two anticyclones on both sides of the equator over the TIO, generated as a response to the equatorial cooling, support the surface equatorial easterlies. The southern anticyclone is not correctly positioned in the model, while northern anticyclone is much weaker. This resulted in the misrepresentation of surface equatorial winds and in turn the north–south mode in the model. The composite analysis is carried out to understand the role of ENSO and IOD on the subsurface mode in CFSv2. The strengthening of subsurface dipole in DJF(0) during El Niño–IOD co-occurrence years is not seen in CFSv2. The rapid decay of TIO SST warming associated with El Niño is seen in CFSv2. The composites of El Niño, IOD and PC1 peak years show that this rapid decay is mainly due to the misrepresentation of subsurface variability in

CFSv2. Correlation and regression analysis shows that the subsurface temperature variability in TIO has major role on the surface temperature variability in TIO along with ENSO and IOD modes. The subsurface–surface interaction is not well captured by CFSv2 mainly during DJF due to the inadequate representation of surface forcing and the deeper thermocline bias in the model. The upward propagation of warm subsurface temperature anomalies amplifies the subsurface surface interaction, whereas such upward propagation is absent or weaker in the model. The weaker subsurface surface interaction weakens the coupled air–sea interaction over TIO resulting weaker feedback on the ENSO evolution. Thus, proper temporal and spatial evolution of subsurface temperature modes in the model might feedback to better SST variability and thereby improving the air–sea interactions. The analysis of CMIP5 coupled model historical

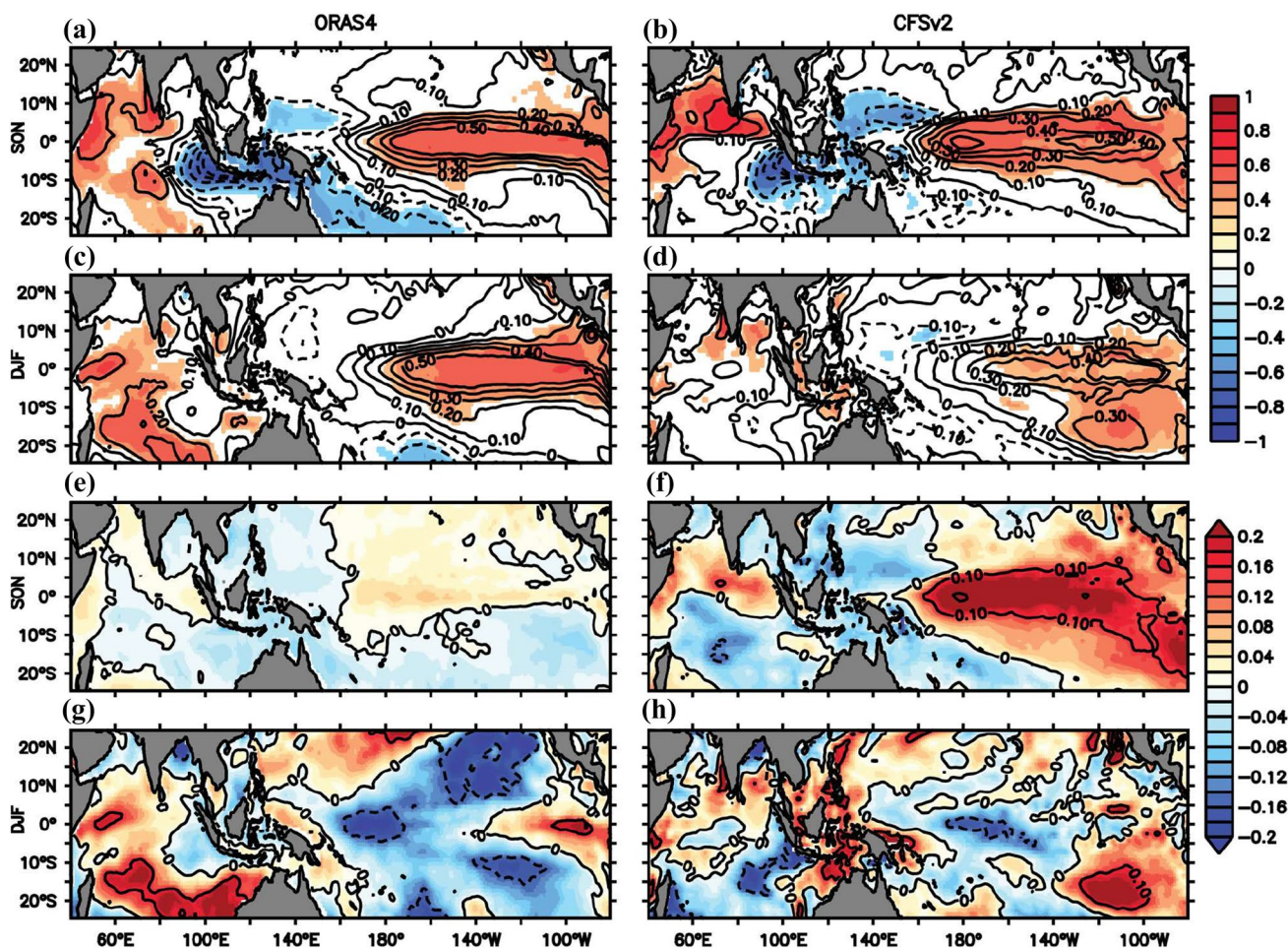


Fig. 15 a–d Correlation coefficient (with 99% confidence level) between PC1 and SST anomalies (shaded) and regression coefficient of SST anomalies regressed against PC1 (contours); SST are averaged over a, b SON and c, d DJF. e, f Composites (shaded) and regres-

sion coefficient (contours) of SST anomalies regressed against PC1 after removing IOD impact g, h composites (shaded) and regression coefficient (contours) of SST anomalies regressed against PC1 after removing ENSO impact

simulations reveal that this improper representation of the subsurface mode is common in most of the coupled models (figure not shown).

Acknowledgements We thank the Director, ESSO-IITM and Ministry of Earth Sciences (MoES), Government of India for support. The comments from two anonymous reviewers helped us to improve the manuscript considerably. We thank M. K. Roxy for providing the CFSv2 free run data. ORAS4 data is downloaded from <http://apdrc.soest.hawaii.edu/>. ERA40 and ERA-Interim data are downloaded from ECMWF website. The ARGO gridded data is available from Asia-Pacific data-research center (APDRC) (<http://apdrc.soest.hawaii.edu/projects/argo/>).

References

- Achuthavarier D, Krishnamurthy V, Kirtman BP, Huang B (2012) Role of Indian Ocean in the ENSO–Indian summer monsoon teleconnection in the NCEP climate forecast system. *J Clim* 25:2490–2508. <https://doi.org/10.1175/JCLI-D-11-00111.1>
- Alexander MA, Bladé I, Newman M, Lanzante JR, Lau N-C, Scott JD (2002) The atmospheric bridge: the influence of ENSO teleconnections on air–sea interaction over the global oceans. *J Clim* 15:2205–2231
- Balmaseda MA, Mogensen K, Weaver AT (2013) Evaluation of the ECMWF ocean reanalysis system ORAS4. *Q J R Meteorol Soc* 139:1132–1161. <https://doi.org/10.1002/qj.2063>
- Balmaseda MA, Hernandez F, Storto A, Palmer MD, Alves O, Shi L, Smith GC, Toyoda T, Valdivieso M, Barnier B, Behringer D, Boyer T, Chang Y-S, Chepurin GA, Ferry N, Forget G, Fujii Y, Good S, Guinehut S, Haines K, Ishikawa Y, Keeley S, Köhl A, Lee T, Martin MJ, Masina S, Masuda S, Meyssignac B, Mogensen K, Parent L, Peterson KA, Tang YM, Yin Y, Vernieres G, Wang X, Waters J, Wedd R, Wang O, Xue Y, Chevallier M, Lemieux J-F, Dupont F, Kuragano T, Kamachi M, Awaji T, Caltabiano A, Wilmer-Becker K, Gaillard F (2015) The ocean reanalyses inter-comparison project (ORA-IP). *J Oper Oceanogr* 8(sup1):s80–s97. <https://doi.org/10.1080/1755876X.2015.1022329>
- Chakravorty S, Chowdary JS, Gnanaseelan C (2013) Spring asymmetric mode in the tropical Indian Ocean: role of El Niño and IOD. *Clim Dyn* 40(5–6):1467–1481. <https://doi.org/10.1007/s00382-012-1340-1>

- Chakravorty S, Gnanaseelan C, Chowdary JS, Luo J-J (2014) Relative role of El Niño and IOD forcing on the southern tropical Indian Ocean Rossby waves. *J Geophys Res*. <https://doi.org/10.1002/2013JC009713>
- Chambers DP, Tapley BD, Stewart RH (1999) Anomalous warming in the Indian Ocean coincident with El Niño. *J Geophys Res* 104:3035–3047
- Chowdary JS, Gnanaseelan C (2007) Basin wide warming of the Indian Ocean during El Niño and Indian Ocean dipole years. *Int J Climatol* 27:1421–1438. <https://doi.org/10.1002/joc.1482>
- Chowdary JS, Gnanaseelan C, Xie S-P (2009) Westward propagation of barrier layer formation in the 2006–2007 Rossby wave events over the tropical southwest Indian Ocean. *Geophys Res Lett* 36:L04607. <https://doi.org/10.1029/2008GL036642>
- Chowdary JS, Parekh A, Kakatkar R, Gnanaseelan C, Srinivas G, Singh P, Roxy MK (2016a) Tropical Indian Ocean response to the decay phase of El Niño in a coupled model and associated changes in south and east-Asian summer monsoon circulation and rainfall. *Clim Dyn* 47(3):831–844. <https://doi.org/10.1007/s00382-015-2874-9>
- Chowdary JS, Parekh A, Sayantani O, Gnanaseelan C, Kakatkar R (2016b) Impact of upper ocean processes and air–sea fluxes on seasonal SST biases over the tropical Indian Ocean in the NCEP climate forecasting system. *Int J Climatol* 36(1):188–207. <https://doi.org/10.1002/joc.4336>
- Chowdary JS, Parekh A, Srinivas G, Gnanaseelan C, Fousiya TS, Khandekar R, Roxy MK (2016c) Processes associated with the tropical Indian Ocean subsurface temperature bias in a coupled model. *J Phys Ocean* 46:2063–2875. <https://doi.org/10.1175/JPO-D-15-0245.1>
- De S, Hazra A, Chaudhari HS (2016) Does the modification in ‘‘critical relative humidity’’ of NCEP CFSv2 dictate Indian mean summer monsoon forecast? Evaluation through thermodynamical and dynamical aspects. *Clim Dyn* 46:1197–1222. <https://doi.org/10.1007/s00382-015-2640-z>
- Dee DP, Uppala SM, Simmons AJ, Berrisford P, Poli P, Kobayashi S, Andrae U, Balmaseda MA, Balsamo G, Bauer P, Bechtold P, Beljaars ACM, van de Berg L, Bidlot J, Bormann N, Delsol C, Dragani R, Fuentes M, Geer AJ, Haimberger L, Healy SB, Hersbach H, Hólm EV, Isaksen I, Kållberg P, Köhler M, Matricardi M, McNally AP, Monge-Sanz BM, Morcrette J-J, Park B-K, Peubey C, de Rosnay P, Tavolato C, Thépaut J-N, Vitart F (2011) The ERA-Interim reanalysis: configuration and performance of the data assimilation system. *Q J R Meteorol Soc* 137:553–597
- Deshpande A, Chowdary JS, Gnanaseelan C (2014) Role of thermocline–SST coupling in the evolution of IOD events and their regional impacts. *Clim Dyn* 1–12. <https://doi.org/10.1007/s00382-013-1879-5>
- Ek MB, Mitchell KE, Lin Y, Rogers E, Grunmann P, Koren V, Gayno G, Tarpley JD (2003) Implementation of Noah land surface model advances in the National Centers for environmental prediction operational mesoscale Eta model. *J Geophys Res* 108(D22):8851. <https://doi.org/10.1029/2002JD003296>
- Feng M, Meyers G (2003) Interannual variability in the tropical Indian Ocean: a two-year time-scale of Indian Ocean dipole. *Deep-Sea Res* 50:2263–2284
- Feng M, Meyers G, Wijffels S (2001) Interannual upper ocean variability in the tropical Indian Ocean. *Geophys Res Lett* 28:4151–4154
- Gill AE (1980) Some simple solutions for heat-induced tropical circulation. *Q J R Meteorol Soc* 106(449):447–462. <https://doi.org/10.1256/smsqj.44904>
- Gnanaseelan C, Vaid BH (2010) Interannual variability in the biannual Rossby waves in the tropical Indian Ocean and its relation to Indian Ocean dipole and El Niño forcing. *Ocean Dyn* 60(1):27–40
- Gnanaseelan C, Vaid BH, Polito PS (2008) Impact of biannual Rossby waves on the Indian Ocean Dipole. *IEEE Geosci Remote Sens Lett*. <https://doi.org/10.1109/LGRS.2008.919505>
- Gnanaseelan C, Deshpande A, McPhaden MJ (2012) Impact of Indian Ocean dipole and el Niño/southern oscillation wind-forcing on the Wyrki jets. *J Geophys Res Oceans* 117(C8):C08005. <https://doi.org/10.1029/2012JC007918>
- Griffies S, Harrison MJ, Pacanowski RC, Anthony R (2004) A technical guide to MOM4. GFDL ocean group technical report no. 5. NOAA/Geophysical Fluid Dynamics Laboratory, Princeton
- Karmakar A, Anant P, Chowdary JS, Gnanaseelan C (2018) Intercomparison of Tropical Indian Ocean features in different ocean reanalysis products. *Clim Dyn* 51(1–2):119–141. <https://doi.org/10.1007/s00382-017-3910-8>
- Klein SA, Soden BJ, Lau NC (1999) Remote sea surface temperature variations during ENSO: evidence for a tropical atmospheric bridge. *J Clim* 12:917–932
- Krishnan R, Ramesh KV, Samala BK, Meyers G, Slingo JM, Fennedy MJ (2006) Indian Ocean–monsoon coupled interactions and impending monsoon droughts. *Geophys Res Lett*. <https://doi.org/10.1029/2006GL025811>
- Lau NC, Nath MJ (2000) Impact of ENSO on the variability of the Asian–Australian monsoon as simulated in GCM experiments. *J Clim* 13:4287–4309
- Masumoto Y, Meyers G (1998) Forced Rossby waves in the southern tropical Indian Ocean. *J Geophys Res* 103:27589–27602
- Rao SA, Behera SK (2005) Subsurface influence on SST in the tropical Indian Ocean: structure and interannual variability. *Dyn Atmos Oceans* 39:103–135
- Rao SA, Behera SK, Masumoto Y, Yamagata T (2002) Interannual subsurface variability in the tropical Indian Ocean with a special emphasis on the Indian Ocean dipole. *Deep Sea Res II* 49:1549–1572
- Roemmich D, Gilson J (2009) The 2004–2008 mean and annual cycle of temperature, salinity, and steric height in the global ocean from the ARGO program. *Prog Oceanogr* 82:81–100. <https://doi.org/10.1016/j.pocean.2009.03.004>
- Roemmich D, Gilson J (2011) The global ocean imprint of ENSO. *Geophys Res Lett* 38:L13606. <https://doi.org/10.1029/2011GL047992>
- Roemmich D, The Argo Science Team et al (1998) On the design and implementation of ARGO: an initial plan for a global array of profiling floats. International CLIVAR project office report 21. GODAE International Project Office, Melbourne
- Roxy M (2014) Sensitivity of precipitation to sea surface temperature over the tropical summer monsoon region and its quantification. *Clim Dyn* 43:1159–1169. <https://doi.org/10.1007/s00382-013-1881-y>
- Saha S, Moorthi S, Wu X, Wang J, Nadiga S, Tripp P, Pan HL, Behringer D, Hou Y-T, Chuang H-Y, Mark I, Ek M, Meng J, Yang R (2014) The NCEP climate forecast system version 2. *J Clim* 27:2185–2208. <https://doi.org/10.1175/JCLI-D-12-00823.1>
- Saji NH, Goswami BN, Vinayachandran PN, Yamagata T (1999) A dipole mode in the tropical Indian Ocean. *Nature* 401:360–363. <https://doi.org/10.1038/43854>
- Sayantani O, Gnanaseelan C (2015) Tropical Indian Ocean subsurface temperature variability and the forcing mechanisms. *Clim Dyn* 44:2447–2462. <https://doi.org/10.1007/s00382-014-2379-y>
- Shinoda T, Hendon HH, Alexander MA (2004) Surface and subsurface dipole variability in the Indian Ocean and its relation to ENSO. *Deep Sea Res Part I Oceanogr Res Pap* 51(619):635. <https://doi.org/10.1016/j.dsr.2004.01.005>
- Srinivas G, Chowdary JS, Gnanaseelan C, Prasad KVS, Karmakar A, Parekh A (2018) Association between mean and interannual equatorial Indian Ocean subsurface temperature bias in a coupled

- model. *Clim Dyn* 50:1659–1673. <https://doi.org/10.1007/s00382-017-3713-y>
- Tozuka T, Yokoi T, Yamagata T (2010) A modeling study of interannual variations of the Seychelles Dome, *J Geophys Res*. <https://doi.org/10.1029/2009JC005547>
- Uppala SM, Kállberg PW, Simmons AJ, Andrae U, Da Costa Bechtold V, Fiorino M, Gibson JK, Haseler J, Hernandez A, Kelly GA, Li X, Onogi K, Saarinen S, Sokka N, Allan RP, Andersson E, Arpe K, Balmaseda MA, Beljaars ACM, Van De Berg L, Bidlot J, Bormann N, Caires S, Chevallier F, Dethof A, Dragosavac M, Fisher M, Fuentes M, Hagemann S, Hólm E, Hoskins BJ, Isaksen L, Janssen PAEM, Jenne R, McNally AP, Mahfouf J-F, Morcrette J-J, Rayner NA, Saunders RW, Simon P, Sterl A, Trenberth KE, Untch A, Vasiljevic D, Viterbo P, Woollen J (2005) The ERA-40 re-analysis. *Q J R Meteorol Soc* 131:2961–3012
- Vaid B, Gnanaseelan C, Polito P et al (2007) Influence of pacific on southern indian ocean Rossby waves. *Pure Appl Geophys* 164:1765. <https://doi.org/10.1007/s00024-007-0230-7>
- Wang B, Wu R, Li T (2003) Atmosphere–warm ocean interaction and its impact on Asian–Australian monsoon variability. *J Clim* 16:1195–1211
- Xiang B, Yu W, Li T, Wang B (2011) The critical role of the boreal summer mean state in the development of the IOD. *Geophys Res Lett* 38:L02710. <https://doi.org/10.1029/2010GL045851>
- Xie S-P, Annamalai H, Schott F, McCreary JP (2002) Structure and mechanisms of south Indian Ocean climate variability. *J Clim* 15:864–878
- Yang J, Liu Q, Xie S-P, Liu Z, Wu L (2007) Impact of the Indian Ocean SST basin mode on the Asian summer monsoon. *Geophys Res Lett* 34:L02708. <https://doi.org/10.1029/2006GL028571>
- Yokoi T, Tozuka T, Yamagata T (2008) Seasonal variation of the Seychelles Dome. *J Clim* 21:3740–3754. <https://doi.org/10.1175/2008JCLI1957.1>
- Yokoi T, Tozuka T, Yamagata T (2012) Seasonal and interannual variations of the SST above the Seychelles Dome. *J Clim* 25:800–814. <https://doi.org/10.1175/JCLI-D-10-05001.1>
- Yu W, Xiang B, Liu L, Liu N (2005) Understanding the origins of interannual thermocline variations in the tropical Indian Ocean. *Geophys Res Lett* 32:L24706. <https://doi.org/10.1029/2005GL024327>
- Zhou Z-Q, Xie XP, Zhang GJ, Zhou W (2018) Evaluating AMIP skill in simulating interannual variability over the Indo-Western Pacific. *J Clim* 31:2253–2265. <https://doi.org/10.1175/JCLI-D-17-0123.1>